Automated Hyperspectral Core Imaging – A Revolutionary New Tool for Exploration, Mining and Research

Martini, B.A. [1], Harris, A.C.[2], Carey, R.[3], Goodey, N.[3], Honey, F.[3], N. Tufilli[3]

1. Corescan Inc., PO Box 58, Denver, CO, 80201, USA
2. Newcrest Mining Ltd., 600 St. Kilda Rd., Melbourne, VIC, 3004, AUSTRALIA
3. Corescan Pty. Ltd., 127 Grandstand Rd., Suite 1, Ascot, WA, 6104, AUSTRALIA

ABSTRACT

The advent of high spatial and spectral resolution hyperspectral core imaging into the minerals industry presages a revolution in quantifiable mineralogical identification and mapping of core, chips, soils and other geological samples from borehole to deposit scales. Technological advances in the past decade, including increased processing capacity combined with precision robotics in high-resolution spectrometers, have resulted in a new generation of high-speed hyperspectral core logging systems becoming available. These multi-sensor platforms integrate reflectance spectroscopy, photography and 3-D laser profiling to generate image and point-based datasets at rates routinely exceeding 400m/day. At 500-µm spatial resolution, 510 spectral bands (from 450-2500nm) and ~200,000 spectral pixels per meter, the Corescan® system represents one such imaging system. Diagnostic absorption features related to molecular scale chemistry and mineral structure are detected and measured in the spectral signatures derived from these hyperspectral imaging systems. Spectral classification and mineral identification algorithms process each spectral pixel and compare the response to an established mineral library. The identification algorithms classify each pixel and determine the relative abundance (or purity) of the minerals present, which is then used to produce visual mineral abundance maps as well as numerical abundance logs. Chemistry and crystallinity parameters can be calculated for specific mineral groups by analyzing spectral absorption features at particular wavelengths. Inherently, this requires large volumes of data storage and significant processing speeds, both of which are now readily available including the ability to provide near real-time processing for mineralogy on-site in operational environments. Application of hyperspectral scanning technology makes deposit-scale petrographic studies possible, provides quantifiable outputs that confirm observations commonly made regarding zonal arrangement of alteration in ore deposits, and can refine and provide new insight into hydrothermal processes and exploration models. Ultimately, this technology provides consistent, objective mineralogical information and refocuses the geologist from being a data collector to a data interpreter and synthesizer. The combination of detailed mineralogical and chemical data in three dimensions on orebody scale promises to deliver new insights into the mineralogical and chemical characteristics, 3-D spatial variability, and genesis of orebodies—case studies from copper porphyry are used to demonstrate these new insights and viability of hyperspectral core imaging.

INTRODUCTION

While spectral based exploration for mineral resource has been operationally deployed since the early 1970's (including space, air and ground-based spectrometers), it is only in the last ~10 years that high spatial and spectral imaging spectrometers have become available for detailed lab-based mineralogical mapping and quantification.

These hyperspectral imagers, as they are also called (a term which denotes 'too many' spectral bands referring to the hundreds of contiguous, spectral bands that comprise such systems) provide a significant step-change in technology from the single-point spectrometers (eg. TerraSpec, ASD Inc.; oreXpress, SpectralEvolution Inc.) relied upon by academia and industry for the last two-plus decades. The individual spectral signatures produced by these point systems are measured over single ~2cm spot sampling intervals, while the newest core imaging spectrometers measure ~200,000 spectral signatures over a single meter of rock/core material (extracted from individual, sub-millimeter, spatially georeferenced and contiguous pixels). Fundamentally, individual spectral signatures, built by hundreds of narrow bands, quantitatively identify mineral species.

When measured by imaging systems, visual mineral abundance maps are generated at both core and deposit scales (hyperspectral core imagers) not unlike the district scale mapping of the earth surface performed since the early 1990's (air and space-based hyperspectral imagers such as AVIRIS, NASA; HyMap, HyVista Pty. Ltd; AISA, Specim Ltd.; Hyperion, NASA). Experiments with handheld spectrometers used to create artificial core images (e.g. Kruse, 1996) paved the way toward the advent of hyperspectral core imaging systems (such as Corescan HCI-III, Corescan Pty. Ltd.; SisuRock, Specim, Ltd.) thus completing the spectral ecosystem; an ecosystem that provides total spectral-based mineral characterisation of mineral deposits from hand-sample to single borehole to whole deposit scales.

High resolution mineralogical mapping from hyperspectral core imaging data allows us to illustrate the spatial distribution of key mineralogical vectors in and around a deposit. This knowledge aids in rapid assessment of exploration models and the development of precise resource domains. Furthermore, deposit-scale mineralogical data can contribute new insights to fundamental hydrothermal and ore formation processes.

BACKGROUND

Digital infrared imaging spectroscopy (or hyperspectral imaging) for identification of earth materials has been in use for over thirty years (Goetz et al., 1985). The individual, single point, lab spectrometers led to full remote hyperspectral imaging systems mounted in aircraft such as the Geoscan Mk II, NASA's AVIRIS and HyVista's HyMap systems (respectively, Lyon and Honey, 1990; Vane et al., 1993; Cocks et al., 1998) and ultimately culminated in the launch of NASA's Hyperion hyperspectral imager on the EO-1 satellite in 2000 (Folkman et al., 2001).

Hyperspectral Imaging

Earth hyperspectral imagers (or imaging spectrometers) identify and spatially map terrestrial materials (rocks, vegetation and artificial constituents) via the collection of both reflected and emitted energy across the electromagnetic spectrum using various detector array configurations and materials. The interaction of this energy (or photons) with earth materials is measured and quantified into spectral signatures whose specific geometries relate to molecular level composition. The ability to collect, geospatially locate and identify spectral signatures consistently is a function of system design including fore-optic engineering, illumination design, calibration (spatially and spectrally), and Signal-to-Noise Ratio (SNR). The ability to characterize, identify and ultimately map millions of hyperspectral pixels is a function of not only the integrity of the original collection of the hyperspectral imaging data but also of the algorithms and software used in identification, analysis and mapping.

The Spectral Signature

As the main building block of the hyperspectral image, the spectral signature extracted from a single pixel (its wavelength extent, geometry and albedo or reflectance magnitude) is carefully measured and characterized using spectral analysis and identification techniques and tools (Figure 1). By definition, the hundreds of narrow, contiguous, hyperspectral bands allow for absolute identification of thousands of earth and artificial materials vs. the simple discrimination and classing of materials afforded by multi-spectral imaging systems (eg. Landsat, ASTER) (Goetz et al., 1985). For example, while a hyperspectral signature can absolutely identify not only chlorite but also the species of chlorite (eg. chamosite vs. clinochlore), multi-spectral systems are only capable of gross mica-class discrimination from other mineral classes such as carbonates or iron oxides (see Figure 1). Furthermore, chlorite is difficult to discriminate from carbonates and most other Mg-bearing minerals (eg. saponite).

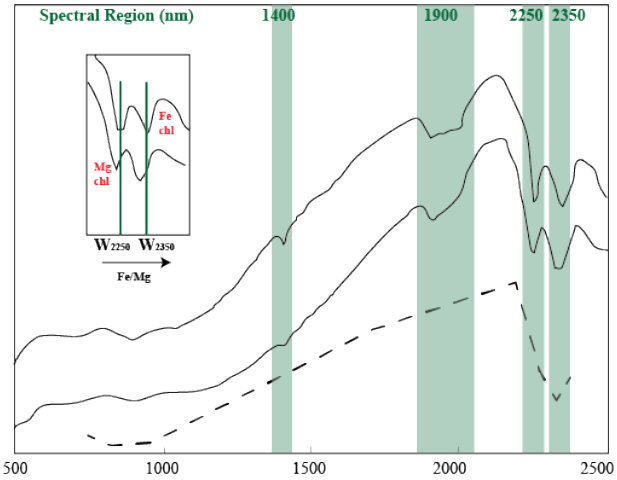

Figure 1: Spectral signatures of two chlorite species, including Fe-rich chamosite and Mg-rich clinochlore (solid lines) measured by the Corescan system; dashed line displays pseudo ASTER signature of chlorite, calculated from deconvolved Corescan spectra. Inset highlights the fine spectral shift of the '2350' absorption feature that identifies specific chlorite chemistry.

Photons (sourced from the sun in air and space-based systems or from artificial illumination in lab-based point and core imagers) interact with material molecules at certain wavelengths that either produce absorptions (due to fundamental electronic shell transitions or molecular bending, stretching and other vibrations and overtones) or reflectance (where the energy at given wavelengths are not compatible with existing chemical compounds within the target material) (Clarke et al. 1990). These collections of absorptions and reflectances form a continuous spectral signature that becomes a unique material identifier. In fact, each spectral signature may even identify multiple materials within a single pixel; a phenomenon referred to as 'spectral mixing'. Such mixed signatures can be analyzed for each individual material and in some cases, quantified or 'un-mixed'.

Large, calibrated spectral libraries are used for material identification, where validation is supplied via other mineral analyses techniques such as thin-section, XRD, SEM, XRF, etc. Widely used examples of such libraries include spectral collections from the USGS and NASA (respectively, Kokaly et al., 2017; Baldridge et al., 2009).

Corescan© HCI-III

This paper focuses on spectral imaging data measured with the Corescan© Hyperspectral Core Imager, Mark III system (HCI-III) which operates across the Visible Near InfraRed (VNIR) and Shortwave InfraRed (SWIR) bands from 450nm-2500nm at an average spectral resolution (or bandwidth) of ~4nm (where the VNIR bands measure at 2.8nm and the SWIR bands measure at 4.5nm). In contrast to the typically irregular sampling of single point systems or the regular sampling, but non-imaging nature of automated point systems such as the HyLogger (Mason and Huntington, 2010), the HCI-III continuously measures the surface of rock material samples at 500 µm spatial resolution (totaling approximately 400Mb/m of imaged core/rock material).

Figure 2: A. Corescan mobile core-logging laboratory at remote on-site project, Fiji, B. Bureau-style Corescan laboratory, Mexico, C. Interior of Corescan laboratory showing sensor module, translation table and processing/server computers for analysis and visualization, D. typical setup during scanning including illumination for hyperspectral imaging (left) and laser profile (right)

High quality optics with directed illumination from dual quartz halogen lamps, focus the spectral measurement to this 500 µm point on the core (Figure 2D), maximizing signal (average 2000:1 across the measured spectrum) and minimizing spectral mixing thus providing a near pure spectral signature at each point on the rock sample (Figure 1 for example HCI-III spectra), with none of the atmospheric or mixing issues inherent to airborne or satellite hyperspectral systems. This results in ~200,000 spectra per meter of scanned rock material.

Spectral calibration, via NIST traceable rare earth reflectance standards, are performed prior to every sample-tray scan and ensure integrity and consistency of spectral data, allowing for comparison of mineral identification and mapping results across global spectral platforms. The system is radiometrically calibrated using Spectralon® reflectance standards and dark current measurements.

In addition, a spectrally calibrated RGB camera provides a high resolution visual record of the core at 50 µm pixel size (Figure 5 for examples). Measurement of core surface features, texture and shape is captured using a 3D laser profiler with a vertical surface profile resolution of 20µm (Figure 2D; Figure 5D). All of these components are housed within the sensor module while a 3-axis translation table allows for tray and rock material management at maximum dimensions of 1.5m long by 0.6m wide (Figure 1C) and a system control module provides high speed data acquisition and processing.

The HCI-III system is housed within a ruggedized shipping container that serves as a mobile core-scanning and analysis laboratory. Able to operate in both regional, bureau-style environments (Figure 2B) as well as in remote, on-site project environments (Figure 2A), the Corescan corelogging laboratory includes the HCI-III system as well as processing computers and mobile servers for facilitation of on-site pre-processing, analysis and distribution/visualization of the co-acquired photography, hyperspectral and laser profile data. Typical scan rates average ~10 minutes/tray while quasi real-time mineral mapping results are available on the Corescan cloud-based, digital archives and visualization platforms in as little as three hours (www.coreshed.com).

METHODS

Spectral characterisation of a mineral prospect/deposit is performed at multiple scales using a combination of hyperspectral core imagery, derived downhole mineral percentage logs, traditional geochemistry and three-dimensional modeling software packages. The goal is to demonstrate the ability of mobile, automated hyperspectral core imaging systems to create deposit-scale petrographic models with quantifiable outputs that confirm zonal alteration arrangements and provide new insight into hydrothermal processes and exploration models.

The Wainaulo Cu-Au porphyry deposits were chosen for the test. Located on the island of Viti Levu in the country of Fiji (approximately 30km west of Suva), the Namosi district served as a remote, but accessible project for testing of the ruggedized Corescan mobile systems. Geologically, the Namosi district also provides challenging mineralogy, assemblages and formation dynamics with subtle alteration vectors, complex and spectrally difficult alteration assemblages (including zoned potassic, calc-sodic and propylitic) and intricate paragenetic relationships including veining, overprints and multiple mineralization phases (both Cu-Fe sulfide and Au) (Ellis et al., 1996).

Core Scanning

A Corescan hyperspectral core imaging laboratory was mobilized to the Namosi district on Viti Levu, Fiji in 2012. The laboratory (run on generator power) was setup in the camp coreshed where historical project core was prepped for scanning by both Newcrest and Corescan team members. The ~17,800 m of historic cut core was cleaned of dust and muds, depth markers checked and overall tray integrity checked before scanning with the Corescan HCI-III mobile hyperspectral core logging system (Figure 2A).

Core trays enter the laboratory and are placed on the automated translation table. The average height of the core material is measured as is the length, width and height of the core tray (though the latter measurement is completed and stored digitally as a template for successive scanning; if core tray size and shape changes appreciably, new dimensions are recorded). All core tray information, including beginning and end depths as indicated on the tray, are entered into the system control computer and scanning is initiated.

Prior to the imaging of each tray, a set of Spectralon® calibration targets are measured including 30% and 70% reflectance targets (for conversion of measured radiance to reflectance and to account for dynamic range) as well as a NIST traceable, REE-doped reflectance standard (for tracking and calibrating spectral band positions).

Spectrally calibrated and spatially co-registered digital RGB photography (50µm spatial resolution) and 510-band

hyperspectral imagery (500µm spatial resolution) are acquired along each row of core (or other rock material). Also acquired simultaneously and spatially co-registered are laser profiles at 20 µm vertical resolution and 200 µm spatial resolution. All three datasets build out in real-time and are visualized within the system control computer (along with real-time monitoring variables for the Corescan system such as internal temperatures, electrical current stability, illumination lamp age, overall measured radiance, etc.). Operators can thus monitor both visual integrity of the data in real-time as well as system specifications (though the Corescan system also automatedly self-monitors and alarms when/if system goes out of spec). All recorded information and specifications (including beginning and end depths of trays) are logged into tray-specific meta-data files. At completion of scanning, data is sent to the in-lab servers for pre-processing; fully georeferenced, spatially co-registered and reflectance-corrected hyperspectral data is available for visualization and spectral query in less than 10 minutes.

The logging of spatial coordinates along with the automated identification and extraction of core sections means visualization of the core and mineral mapping products are immediately available in a spatially referenced context, overcoming the time-consuming image reconstruction overhead associated with traditional core tray imaging approaches. Core is scaled and reconstructed in real time even when core recovery is less than 100%.

Once the data has been pre-processed, including a full QC of all spectral and spatial parameters by the on-site technicians, the data is transferred to Corescan spectral geologists for further spectral processing and analysis.

Corescan Data Analysis

A full suite of QC assessments and spectral/spatial analyses are performed by the Corescan engineering and geological teams. Quality assessments include both spatial and spectral/radiometric integrity tests and are specifically aimed at image quality. The checks are followed by a series of spectral and textural analyses and interpretations performed on both the hyperspectral and laser profile datasets.

Hyperspectral Image Analysis

Hyperspectral image datasets (or data cubes as they are also called, alluding to the spatial x-y-z dimensionality which refers to the image spatial x-y character and 'vertical' z dimensionality of the 510 spectral bands) are brought into proprietary Corescan spectral analyses software (Chameleon™) and analyzed with a suite of project specific algorithms which aim to both identify and spatially map mineralogy.

Masking of non-core material (i.e. core trays, depth blocks and any other preparation material or refuse) is performed prior to spectral mineralogical analyses. Analysis of remaining pixels is initiated by running spectral matching algorithms that compare extracted Corescan spectra against known, validated spectral libraries such as the USGS Speclib07 (Kokaly et al., 2017) and internal Corescan spectral libraries built up over the last decade. These total a collection of ~3000 minerals, mineral sub-species and other materials (e.g. tray materials, drilling muds, organics/hydrocarbons). The Corescan software allows for bespoke selection, by the spectral geologist, of diagnostic spectral absorption, slope and shoulder features – not just the currently known spectral behaviors of individual mineral species. This functionality allows the spectral geologist to identify not only wider ranges of behavior within mineral species (due to things like cation/anion replacements, crystallinity changes, intra-crystalline water additions, etc.) but to also identify mineral mixing at sub-pixel resolutions which delivers a more accurate identification and quantification of mineral species.

Through several analysis and processing iterations (which includes identification of dominant and trace mineralogy as well as test-mapping to determine spatial mapping completeness), the spectral geologist distills the hyperspectral imagery into a project-specific spectral library. This initial spectral iteration is performed on orientation core (one or two boreholes that represent known geology/alteration and/or specific core intervals thought to represent dominant geology/alteration) and then applied throughout the entire project.

The spectral signatures from each pixel are compared to the project spectral library and two levels of classification are performed: 1) the presence or non-presence of project minerals within the core (from the project spectral library) are mapped into visual abundance images called Match Images (Figure 3B,C; Figure 5) – where purity within each pixel (i.e. how good of a match the pixel spectral signature is compared to the library spectra) is thresholded at no lower than 92% match and is color-coded with a rainbow gradient from blue (lower match) to red (higher match) and 2) Mineral Classification maps which display the occurrence of all detected minerals in a single image map with corresponding mineral key (Figure 5). It should be noted that multiple Mineral Classification maps are typically created to study different mineral and mineral assemblage behaviors (e.g. a Mineral Classification map that shows only mica species or only sulfates). It should also be noted that as a single 500 µm pixel may contain multiple minerals, the Mineral Classification maps are created with mineral decision-tree organization (where the spectral geologist sets up rules to determine what minerals to plot within the Mineral Classification maps based on desired analysis and visualization goals).

In addition to identification of project mineralogy, compositional information is extracted and mapped (which includes chemical compositional differences such as Mg vs. Fe-rich chlorite [Figures 1,3 and 5B,C]) and mineral structure information (which includes identification of both amorphous behavior as well as identification and classification of degree of "ordered-ness" or crystallinity). These compositional (and crystalline characterisation images where calculated) are displayed similarly to Match Images with a rainbow gradient color scheme applied to delineate changes in wavelength due to chemical changes (Figures 3, 5).

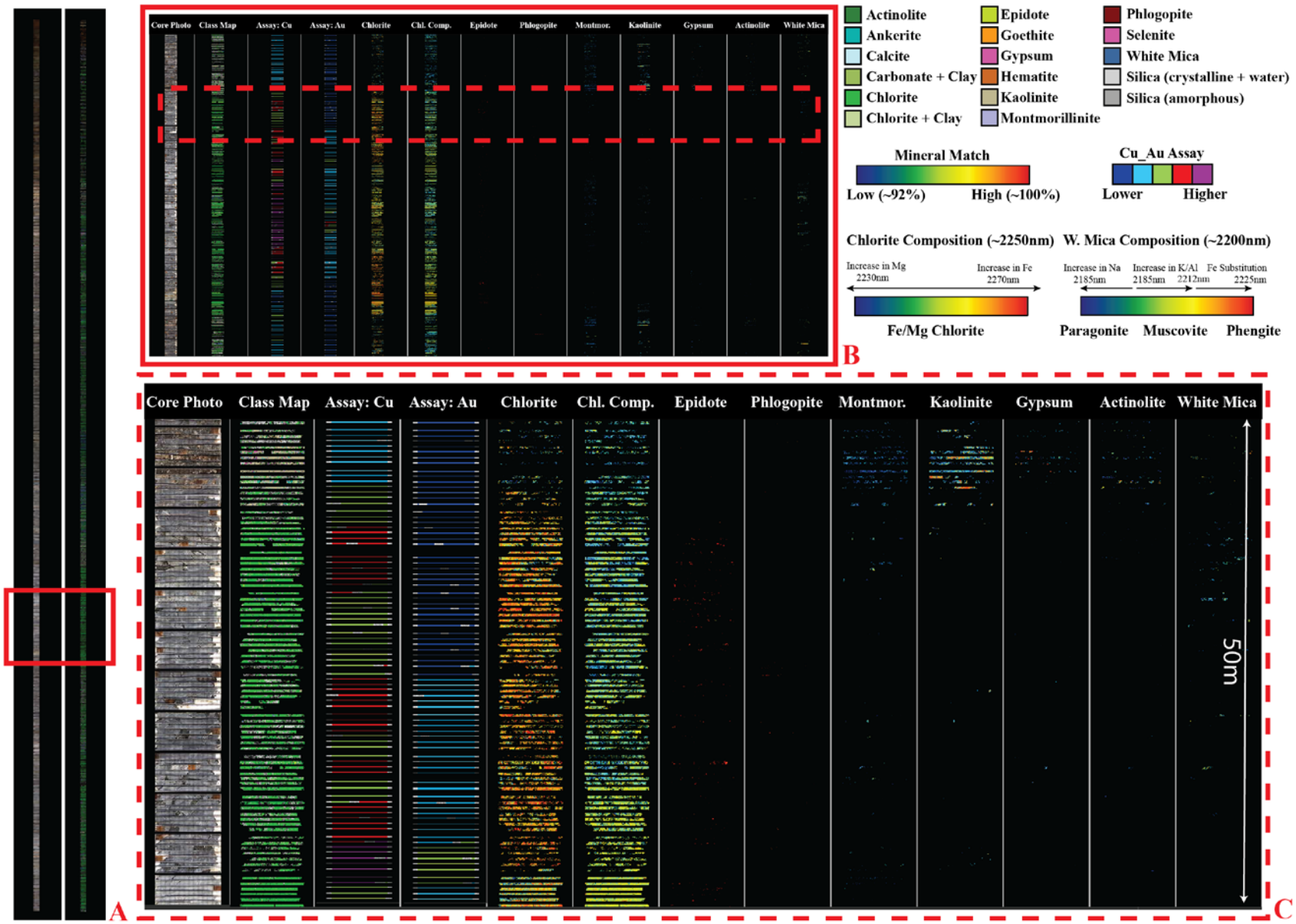

Figure 3A. True color, digital 'stacked section' image (left) and mineral classification map (right) of Wainaulo borehole NVD007 (894m TD), B. Tighter spatial interval highlighting distribution of mineralogy, mineral composition, Cu and Au assay, C. Zoomed-in view of mineralogy directly preceding high Cu grades; sharp alteration boundaries (montmorillinite + kaolinite + gypsum + actinolite) are highlighted as well as the clear increase in chlorite abundance and changing chlorite composition towards the iron-rich species (chamosite) in more mineralized zone

These spectral analyses are performed at rates of >1,000 spectra per second on 16 parallel servers and stored on over 100Tb of processing storage. At ~17,800 m of core, over 3.5 billion spectra were processed, identified and mapped for the Namosi dataset.

Laser Profile Image Analysis

Concurrent with collection of digital RGB photography and hyperspectral data, is the collection of laser profiles at 20 µm vertical resolution (and 200 µm spatial resolution). The laser profiler scans continuously along the surface of the core and is visualized as a full core/sample image in grey scale (Figure 5D). This simultaneous surface measurement allows for the detection and quantification of simple geotechnical variables (breaks per meter, surface roughness and RQD) and structural variables (fractures, fracture set-spacing and fracture orientation) using separate algorithms for detection and mapping of surface height variability and relative variation. Although standard output, the Namosi project laser profile data was not the focus of the study.

Semi-Quantitative Downhole Mineral % Logs

While the imagery and mineral classification images produce informative spatial information for logging, paragenetic studies and geotechnical assessments, ultimately the distillation of image data into downhole mineral percentage logs produce the semi-quantitative input for statistical analyses and three-dimensional modeling. We say semi-quantitative as only exposed surfaces are mapped (i.e. not whole-rock measurements) and some rock forming minerals are invisible to spectroscopy in the SWIR range

Downhole mineral percent logs are calculated based on a given interval (at 1 m intervals for the Namosi project – but possible at any desired depth interval down to 2cm). Total number of pixels

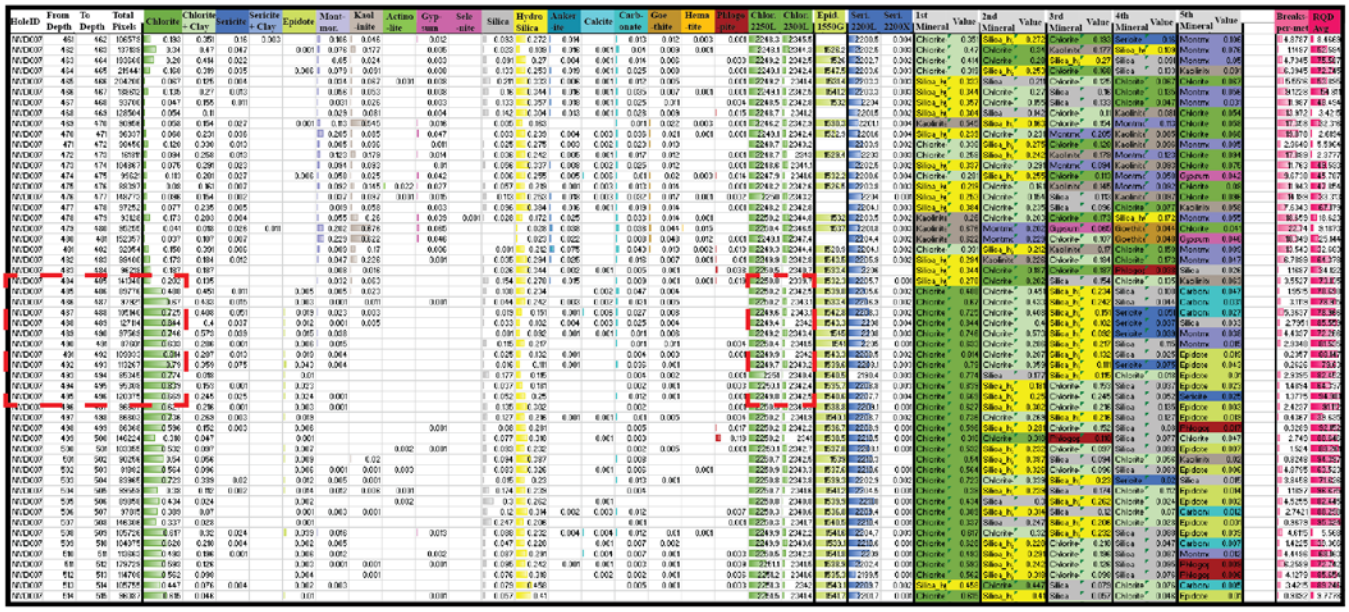

HoleID	From Depth	To Depth	Total Pixels	Chlorite %	Chlorite Composition (2250L)	Chlorite Comp. (2300L)
NVD007	484	485	141348	0.202	2250.769	2339.734
NVD007	485	486	89776	0.488	2250.188	2342.466
NVD007	486	487	97921	0.67	2250.235	2343.052
NVD007	487	488	105140	0.725	2249.572	2343.129
NVD007	488	489	127114	0.844	2249.364	2341.989
NVD007	489	490	97569	0.746	2249.169	2343.353
NVD007	490	491	87601	0.633	2250.432	2341.491

Figure 4. Semi-quantified downhole mineral percentage logs taken from a short interval (461-515m). Each mineral abundance was computed for a single, one meter interval and includes percentage of each identified mineral, mineral composition wavelength values, dominant minerals as proxy for assemblage and geotechnical variables derived from the laser profiling data; bottom image shows detailed tabulation example for chlorite and its composition

across the rock sample/core surface, in a given interval, are tabulated. In the given interval, the total number of pixels of each identified mineral are tabulated and divided through by the total amount of pixels in said interval. This division produces a specific mineral percent at each interval and is stored in simple .csv files (Figure 4). The total pixels per interval as well as unclassed pixels are also counted and are used together with the pixel counts of individual minerals to normalize all mineral pixel counts to add up to 100%. Unclassed pixels include those pixels where the spectra are either too noisy due to mineral crystal orientation or minerals are too dark and reflect minimum light.

In addition to mineral percent at a given interval, compositional and crystallinity information is reported as are the measured geotechnical and structural data from the laser profile data (Figure 4). All of these data are exported as stand-alone .csv files (for import into databases, statistical and modeling software) and displayed within the Coreshed® online virtual coreshed for comparison with spatial imagery, Match Images and Classification Maps (Figure 3,5).

Visualization

Visualization of mineral mapping results from the 21 drill holes of 17,800 m of scanned and analyzed core was facilitated by both an on-line, virtual core repository and by import and display of point data within three-dimensional modeling software.

On-Line Virtual Coreshed

The depth of the drill holes (all Namosi holes are at least 350 m deep with the majority over 600 m deep and five holes at greater than 1000 m deep) makes vertical visualization within the limitations of digital screens challenging. Viewing individual trays or small core/sample sections, similar to manual logging techniques and viewing norms, is straightforward (see Figure 5 for examples) – however digitally viewing the intricate mineralogical patterns and intervals over a 1000 m of vertical core is impossible without some digital visualization treatments.

Corescan has designed an online viewing platform for the virtual storage and visualization of scanned core (digital RGB photography) and the mineral and surface mapping results (hyperspectral and laser profile data). This virtual repository, Coreshed®, displays scanned and analyzed core in not only a digitally reconstructed, vertical borehole format (short intervals in Figure 5) but also in a so-called, 'stacked-section' format which displays individual core trays stacked vertically with depth, downhole (Figure 3A,B,C). This stacked section mode provides an abbreviated depth profile that allows geologists to more easily observe and analyze mineralogical patterns with depth, and to compare spatial locations of individual mineral species throughout entire boreholes (as well as compare with other imported point data such as assay) (Figure3B,C).

All data is visually co-registered allowing for comparison between higher resolution digital RGB photography and hyperspectral-based Mineral Match and Classification Maps – even allowing for real-time overlays of data (Figure 5A,B,C) and live-updating mineral keys for Classification Maps.

The virtual Coreshed is hosted at on-line servers globally and is accessible to registered users via a web-based interface with username and password protected access protocols. The digital repository is available 24 hours a day, 365 days a year and serves as a reliable core curation strategy (over and above physical core storage).

Three-Dimensional Modeling

Viewing not just individual borehole mineralogy but entire deposit geology is a key element of geological and mine development modeling. The downhole mineral percentage logs generated from Corescan data are brought into typical three-dimensional modeling software via .csv files that contain drill hole collar locations (including orientation data if available), depths and selected mineral component percentages.

Once imported (along with other geological information such as mapped lithology, structure and assay), the mineralogical data can be viewed from multiple angles and various geological and mineralization associations tested. In combination with mineral assemblages and potential mineralization vectors ascertained from interrogation of photos and mineral maps from Coreshed, likely alteration and lithology shells are constructed within the three-dimensional model and tested with respect to known mineralization. Secondary, revised alteration and lithology derived from this process is compared to original geological models with potential derivation of tertiary models that incorporate both original and modified geology. The process continues until a geological stasis is reached and a model is arrived at for future testing via more drilling or other suites of testing and analyses.

RESULTS

While not feasible to display representative results for all 17,800 m of core, the mapping results from a single borehole (NVD007) were chosen to represent the dominant mineralogical findings. This borehole cuts through all major lithologies, alteration assemblages/zones and passes through both low and high grade within the Namosi project. The results from hyperspectral analysis and mapping at fine intervals demonstrate small scale mineralogical characteristics, paragenetic relationships and assemblages (Figure 5) while scaling up to the full borehole demonstrates larger mineralogical patterns (both lithological and alteration-focused) and reveals mineralization vectors (Figure 3). The sum total of all mineralogical mapping for each of the 21 boreholes is then visualized in three-dimensional space, which reveals large-scale mineralogical patterns that constrain the geological model and define grade (Figures 5).

Hyperspectral Analysis

Hyperspectral processing and analysis of the 17,800 m of core revealed 16 separate minerals including actinolite, ankerite, bornite, calcite, chlorite, epidote, goethite, gypsum, hematite, hydrous silica, kaolinite, montmorillinite, phlogopite, white mica, selenite and silica (crystalline with free water) (Figure 3).

A gross carbonate class was also mapped (to capture broader alteration patterns and fundamental lithology). This class includes both of the separate species of ankerite and calcite.

During spectral processing and analysis, several consistent mineral mixtures (recognized by the presence of two or more diagnostic mineral absorption and slope features within a single spectral signature) were noted including white mica + goethite and two general clay mixtures with both carbonate and chlorite (carbonate + clay; chlorite + clay). While clay species are typically defined specifically (as seen in the current mineral classes for Namosi which include separate identification of both kaolinite and montmorillinite), the mapped clay mixtures simply indicate the presence of clay-bearing hydroxyl molecules with no attempt to discern specific clay species.

All identified minerals were collected into a single classification map where the vast majority of pixels were assigned a mineral (with corresponding color) based on the spectral signature identification (Figure 3). Un-identified pixels remain un-classed or black in the final classification maps. As discussed previously, numerous minerals may reside in a single 500 µm pixel and thus the classification mapping scheme has a logical decision tree-type approach whereby the identified Namosi project minerals are assigned priority rankings based primarily on abundance. For example, the far less abundant phlogopite class is placed at a higher priority than chlorite (Figure 3C clearly shows the vast difference in abundance); in practice, this equates to the 'coloring' or classing of a pixel as phlogopite, if both phlogopite and chlorite occur in the same pixel. It is important to note that this scheme does not ultimately affect mineral logs as only the mineral match images are used to calculate downhole mineral percentages.

In addition, structural and chemical compositional characteristics were identified and mapped in four of the seventeen separate minerals classes (which includes the gross carbonate class). Epidote composition (based on the position of the ~1540 nm absorption) (Roache, et. al., 2011), white mica composition and crystallinity (based on the position and depth of the ~2200 nm absorption feature) (Scott, 1977), chlorite composition (based on the position of both the ~2250 nm and ~2300 nm absorption features and shown visually in Figure 3) (McLeod et al, 1987) and carbonate composition and crystallinity (based on the depth and position of the ~2300 nm absorption feature) (Gaffey, 1984). These wavelength values represent an average location of these diagnostic spectral absorption features, where individual spectral minima may shift approximately ~20 nm on either side depending on composition. For example, chlorite may range from ~2230nm (Mg-rich) all the way through to ~2270nm (Fe-rich) (see Figure 1) (McLeod, et al, 1987).

Each of the identified minerals (including compositional and structural characteristics) are visualized as a single mineral match image where the rainbow color gradient corresponds to either goodness of fit to the Namosi project spectral library (individual mineral maps shown in Figures 3 and 5) or to some calculated characteristic (e.g. colors corresponding to specific changing wavelength values such as those shown for chlorite in Figure 3 or 5B,C).

NVD007

The borehole NVD007 was drilled through the major lithologies present at the Wainaulo prospect, within the Namosi district. The entire borehole is approximately 894 m total depth (displayed in its entirety in Figure 3A) and passes through Miocene-age, andesitic, volcanic and volcaniclastic units of the Namosi Andesite Formation, late Oligocene to middle Miocene basaltic andesite volcanics and volcaniclastics of the Wainimala Group and medium-K, calc-alkalic porphyritic rocks that intrude both Groups (specifically dioritic plutons and dike complexes at Wainaulo) (Ellis, 1996; Orovan, 2016).

The alteration at Wainaulo is complex, with multiple phases of alteration and mineralization. All of these phases are captured in the hyperspectral imaging data, including some previously undefined minerals and mineral compositions within the alteration assemblages as well as a better definition of alteration shell location, shell boundary and relationship to inception of mineralization (i.e. better vector and grade definition).

The proximal, early phases of mineralization (hosted within the porphyritic, diorite plutons and localized around vertically attenuated dikes), are associated with biotite + albite + magnetite + actinolite +/- muscovite +/- rutile with chalcopyrite +/- molybdenite (Orovan, 2016). Hyperspectral-based mapping captures this alteration assemblage via identification of phlogopite (biotite), actinolite and white mica (both muscovite and phengite as seen in the white mica composition image in Figure 5A). The mapped mineralogy from this early phase is weaker than in all other zones (and is dominantly vein-associated), as much of this older, primary mineralogy has been overprinted at least once. Indeed, even this short interval bears a chloritic overprint (seen both in the last panel and as an overlay on core photography in the first panel of Figure 5A).

Note that albite is spectrally inactive in the 450-2500 nm wavelength range covered by the HCI-III, and thus is not identified in this study. Note also that the dark mica mapped at this project is called phlogopite (the Mg-rich endmember), however much of the dark mica is likely biotite (derived from thin-section analysis). Biotite can be identified in hyperspectral data, however spectral mixing, alteration and overprinting processes can make it challenging. In this project, we have chosen to conservatively identify the spectral endmember as phlogopite, however its distribution through the deposit is used as proxy for the biotite that is identified through other methods. Similarly, magnetite is normally identifiable in hyperspectral data, however the fine-grained nature of the magnetite in this project made detection difficult with higher than acceptable errors of omission; hence it was eliminated from the final classification maps. While magnetite is often an excellent Cu-vector and thus an important target for identification, other mineralogy (specifically chlorite) was found to be an excellent vector for Cu in this project, discussed further in the following section.

Early stage mineralization is followed by the main stage mineralization that was initiated with quartz diorite intrusions (demonstrated by detailed age-dating studies; Orovan, 2016). This mineralization (primarily hosted in quartz + magnetite +

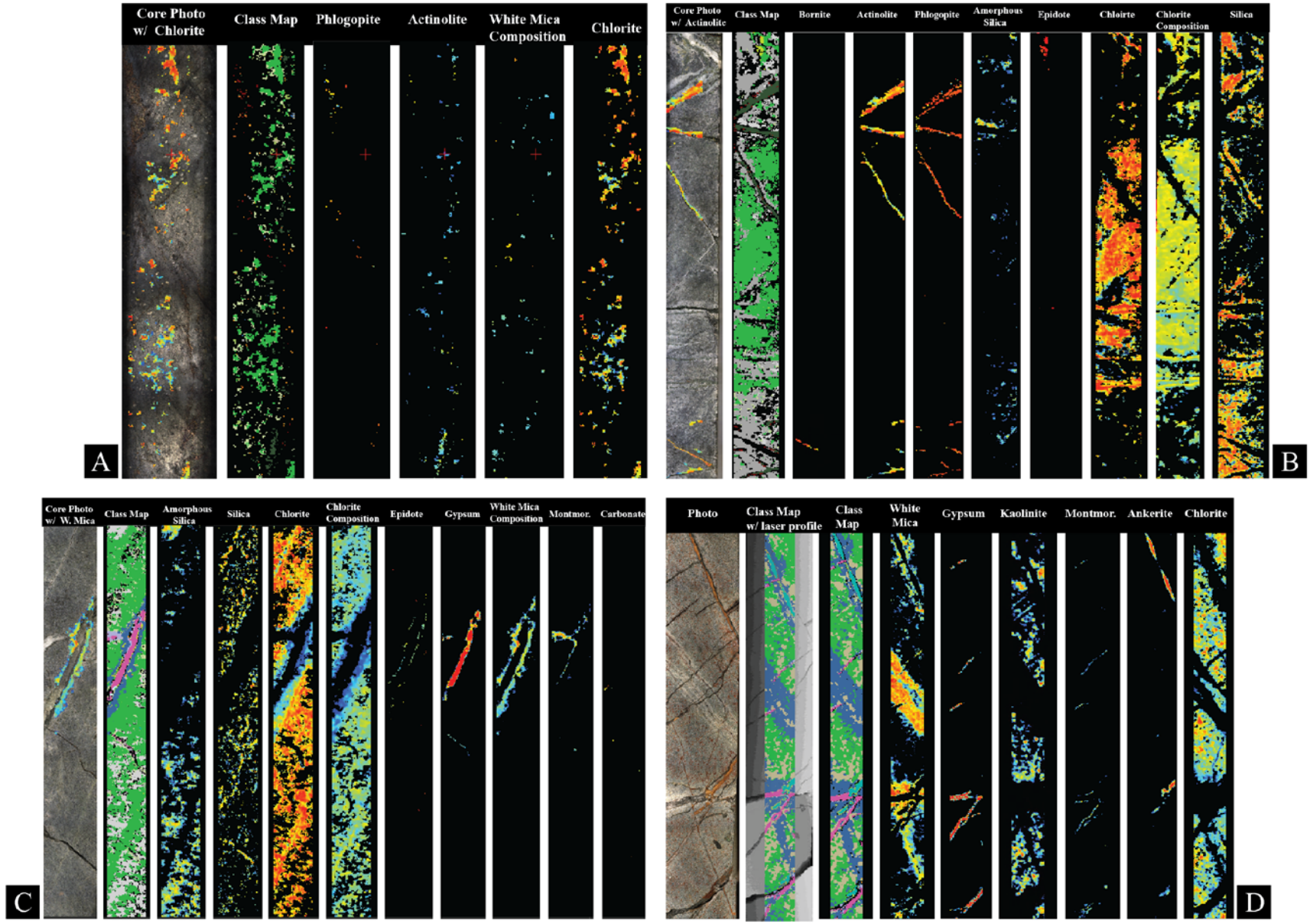

Figure 5A. Short interval of core (~20cm in length) that maps the alteration associated with the early stage of mineralization, namely phlogopite + actinolite + white mica with incipient chloritic overprint, images from left to right include photography with overlaid chlorite match image, classification map and match images with each identified mineral in this interval B. Approximately 30cm of core taken from the main stage mineralization zone that highlights extensive chlorite and silica overprints along with cross-cutting veins of actinolite + phlogopite + amorphous silica and a single bornite vein, C. Approximately 25cm of core that highlights the secondary vein overprints of the primary mineralization-bearing chlorite, including epidote + gypsum with white mica and montmorillinite halos and D. a short interval (~20cm) of core that highlights structurally focused alteration including pervasive kaolinite and chlorite cut by gypsum, montmorillinite, ankerite and white mica bearing fractures in two different orientations

bornite and quartz-sulfide veins) is accompanied by a significant overprinting event, exemplified by a chlorite + albite + quartz + actinolite + epidote assemblage (Orovan, 2016). This assemblage is mapped in the hyperspectral data as a combination of chlorite + actinolite + epidote + silica (both amorphous and crystalline). Some of the original biotite veins are captured (mapped as phlogopite) as well as a single bornite vein (Figure 5B). While both silicas appear as selvages of the phlogopite + actinolite veins, the more crystalline silica (which still has some weak water absorption features indicative of amorphous behavior) does exhibit some pervasive character as well. The chlorite is dominantly pervasive, intermediate in composition and clearly cut by the phlogopite + actinolite + silica (+ epidote) veins, revealing a more detailed paragenesis than previously recognized.

The main stage of mineralization (and accompanying alteration) is ultimately overprinted by a set of epidote + sulfide + anhydrite + calcite + hematite veins with kspar + epidote + phengite vein halos (Orovan, 2016). These veins are recognized in the hyperspectral data and dominantly present as gypsum with epidote + white mica +/- montmorillinite selvages (Figure 5C). Note that while gypsum and anhydrite have distinct spectral signatures, absolute discrimination between the two is rarely possible in the VNIR-SWIR wavelengths as hydration during/after drilling may lead to alteration of the primary anhydrite to gypsum. Mineral assemblage and lithology allows for identification of the $CaSO_4$ in this core (and the greater deposit) as anhydrite, however as the spectral signatures contain H_2O absorption features, we have maintained the identification as gypsum in the classification and match images. The white mica selvage is clearly mapped as a halo around the gypsum (anhydrite) vein and is compositionally trending from muscovite into phengite (where phengite appears redder in the white mica composition image in Figure 5C). Additionally, the presence of montmorillinite as selvage (with the white mica) may represent alteration of previously recognized halo kspar (from Orovan, 2016).

These veins cut the pervasive chlorite alteration, which is trending from intermediate chlorite chemistry (Mg ≈ Fe) directly adjacent to the veins, to more Fe-rich (chamosite) away from the veins (where iron is likely taken up by sulfide formation within the vein sets) (Figure 5C). Finally, while the silica is dominantly pervasive in character (and appears to be cut by the gypsum veins), there is evidence that it too post-dates the chlorite, either as selvage to the anhydrite veins (some linear, vein-like patterns appear in the silica maps in this interval), or as a later-stage, pervasive alteration that washed through prior to the gypsum vein overprinting event.

Additionally, a set of structurally-focused alteration is mapped in this deposit that is primarily characterized by illite + muscovite + anhydrite + calcite + pyrite and kaolinite + montmorillinite + ankerite +/- hematite with ubiquitous chlorite + illite/smectite overprints (Orovan, 2016). Extensive fracturing and brecciation textures are mapped within the imaged project core, seen both mineralogically and via the laser profile images (example interval shown in Figure 5D). White mica (compositionally muscovite) is mapped cross-cutting pervasive chlorite and kaolinite while at least two different fracture orientations are mapped with gypsum + montmorillinite + ankerite in-filling one set and a separate orientation of fracture-filling ankerite. At larger scales, pervasive kaolinite and partially veined and pervasive montmorillinite immediately precede mineralized Cu zones (Figure 3C).

Moving from individual core scale hyperspectral alteration maps up into the entire borehole scale, reveals larger alteration patterns that match previously understood alteration assemblages and paragenesis as well as deviating in some important ways. As previously noted, the primary and earliest stage potassic-phase mineralization does coincide with mapped phlogopite (seen weakly in Figure 3C matching the highest Cu-assay values colored in red and purple). The subsequent overprints, particularly those associated with the main stage of mineralization, are well correlated to the vertical distribution of both epidote (+/- white mica) and chlorite in the hyperspectral data (Figure 3C).

However, a few different alteration behaviors are noted in the hyperspectral data that modify and improve our understanding of paragenesis and vectors to mineralization in the Wainaulo deposit. The chlorite + albite + epidote + calcite +/- montmorillinite +/- magnetite assemblage has been previously noted peripheral to the main mineralized zones with the addition of actinolite and the weakening of montmorillinite and epidote as the main ore zone is approached (Orovan, 2016). While the hyperspectral analysis does indeed show a significant weakening of montmorillinite as the main Cu-ore zone is approached (see both Figure 3B and C), it also highlights that the presence of actinolite is quite strong preceding the ore zone, and falls significantly as the Cu-ore zone is entered. The previously discussed main-stage overprint that includes chlorite, albite, quartz, actinolite and epidote is certainly present in the ore zone, however visualizing all of the actinolite in the borehole allows us to quantify overall abundance better and to discriminate actinolite alteration associated with increased Cu deposition from un-mineralized pervasive actinolite alteration. The sharp boundary between the low-grade Cu-zone actinolite and the higher-grade actinolite zones (and the coincidence of this boundary with significant decreases in montmorillinite abundance) also allow us to construct more detailed alteration shells. Note that the presence and coincidence of kaolinite in this alteration shell boundary transition was previously unknown and reinforces our understanding of strong mineralogical changes at the inception of higher grade Cu enrichment (Figure 3B,C). The sharp mapped boundaries highlight both the inception of high grade zones, as well as the termination – allowing for very detailed, accurate measurement of high-Cu associated alteration and ultimately better geological models.

While the high Cu-grade zone is well bracketed by montmorillinite + kaolinite + gypsum + actinolite +/- white mica (Figure 3C) and coincides with the presence of epidote + phlogopite +/-montmorillinite +/- kaolinite +/- gypsum +/- actinolite +/- white mica, it is the chlorite and chlorite composition that reveal previously unknown alteration behavior as related to mineralization (both Cu and Au). The plots shown in Figure 3C demonstrate that the presence of chlorite (as part of the main-stage overprint associated with mineralization) is confirmed – but more importantly there is a significant increase

in abundance at the inception of higher Cu-grade as well as a shift in composition from intermediate to more iron rich (chamosite) chlorite within the higher grade Cu-zone. Additionally, while NVD007 does not contain significant Au, the one interval with elevated gold (near the bottom of Figure 3C) is also the zone with the most iron-rich chlorite (which also corresponds to the highest Cu-grades in this interval). Ultimately, the main-stage, mineralized overprint of the primary potassic suite of phlogopite + actinolite (as measured by hyperspectral), is measured by the abundance and composition of chlorite (+ epidote). Semi-quantification of this measured mineralogy and visualization across all boreholes in three-dimensions reveals a better-defined geological model and ability to better vector to higher grade Cu.

Three-Dimensional Modeling

The consistent collection of ~200,000 spatially referenced pixels per meter of imaged core allows for semi-quantification of the previously discussed imaging and mineral mapping results. The ~3.5 billion pixels (over 17,800 m of core within 21 boreholes) were classified and counted over intervals of one meter. These semi-quantitative point-counts ('semi' due to the single-side, non-whole rock nature of hyperspectral core imaging) were collated into simple .csv files. Figure 4 shows a short 54m interval from the NVD007 borehole with all identified mineralogy reported at one-meter intervals. The values for each identified mineral are reported in a percentage which represents the division of total counted mineral species divided by total amount of imaged pixels over that same one-meter interval (see bottom of Figure 4 for closer view of reported values). A ranking was calculated that lists the first through the fifth most abundant minerals within each one-meter interval (thereby providing a quick idea of assemblage in each interval). Geotechnical variables extracted from the laser profile data (such as the image shown in Figure 5D) are also reported per meter interval (including RQD and Breaks-per-Meter).

Note that compositions are also quantified for specific mineral species (reported as the average measured wavelength value for each compositional parameter). For instance, chlorite composition (from Mg to Fe-rich species) is tracked by the shifting of the 2250 and 2350 nm wavelength (L) positions, and collated downhole. These chlorite composition data, across all 21 boreholes, were then plotted in three-dimensional block diagrams using 100-meter voxel resolution (see Figure 6). The colors correspond to the actual measured chlorite composition, where reds and pinks indicate more iron-rich chamosite and the blues indicate more Mg-rich clinochlore. As noted in the previous section, Cu-grades vector strongly with the more Fe-rich chlorites associated with the main-stage mineralization front that altered and overprinted the primary biotite-rich potassic zone. The distribution of Fe-rich chlorites is thus accepted as an accurate, consistent vector for high Cu-grades and when mapped over the Namosi district (including both Wainaulo where NVD007 was drilled, but also extended east to the associated Wasoi deposits), gives a better-defined map of Cu mineralization (where higher grades are found to be shallower at Waisoi and deeper at Wainaulo).

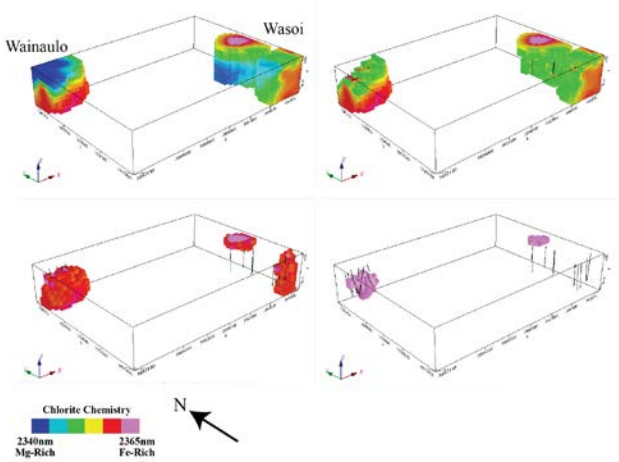

Figure 6. Three-dimensional modeling across the Namosi district (including both the Wainaulo and Wasoi deposits) showing the distribution of chlorite as represented by 100m voxels based on the 21 drill holes of hyperspectral data. The colors represent chlorite composition and demonstrate that more Fe-rich chlorite (chamosite) vectors towards higher copper grades at depth for Wainaulo and is shallower in the Wasoi project.

CONCLUSIONS

Though hyperspectral imaging has been in viable commercial use for almost thirty years, the increased processing capacity and speed, precision robotics, high resolution spectrometers, high speed scanning and large volume data storage afforded by such systems as the HCI-III have made large volume (~tens of thousands of meters of core) scanning and interpretation possible. Automated, multi-sensor platforms (such as the geospatially linked photography, hyperspectral imaging and laser surface profiles of HCI-III) free the traditional data collectors (coreshed geologists) and turn them into data interpreters and synthesizers.

Portable, high-resolution hyperspectral core imaging deployed at the Namosi project provided consistent, accurate mapping and quantifiable mineralogical outputs that confirmed previous observations made regarding the zonal arrangement of alteration in this Cu-Au porphyry deposit. Both early and main stage mineralization events were captured (via associated alteration assemblages) as were subsequent overprints and peripheral/distal alteration suites. Additional alteration behaviour not previously known was identified including most importantly the strong correlation between Cu-grade and the iron-rich chloritic overprints of the primary biotite (phlogopite)-bearing potassic core of the porphyry. This knowledge aided in rapid assessment of the exploration model via scaling single borehole results up through the entire Namosi district via three-dimensional modelling and the development of precise resource domains. Furthermore, these deposit-scale mineralogical data contributed new insights into fundamental hydrothermal processes and basic paragenesis.

REFERENCES

Baldridge, A.M., S.J. Hook, C.I. Grove, G. Rivera, 2009, The ASTER Spectral Library Version 2.0: Remote Sensing of Environment, 113, 711-715.

Bierwirth, P., D. Huston, R. Blewett, 2002, Hyperspectral Mapping of Mineral Assemblages Associated with Gold Mineralization in the Central Pilbara, Western Australia: Economic Geology, 97, 819-826.

Clarke, R.N., T.V.V. King, M. Klejwa, G.A. Swayze, 1990, High spectral resolution reflectance spectroscopy of minerals: Journal of Geophysical Research, 95, 12653-12680.

Cocks, T.D., R. Jenssen, A. Stewart, I. Wilson, T. Shields, 1998, The HyMap Airborne Hyperspectral Sensor: The System, Calibration and Performance in the Proceedings of 1st EARSEL Workshop on Imaging Spectroscopy, Zurich.

Ellis, P.D., 1996, The Geology and Mineralisation of the Waisoi Porphyry Copper Deposits, Namosi Province, Republic of Fiji: MSc Geology, Codes Key Centre, University of Tasmania, 211p.

Folkman, M.A., J. Pearlman, L.B. Liao, P.J. Jarecke, 2001, EO-1/Hyperion hyperspectral imager design development, characterization and calibration in Proceedings SPIE, 4151, 40-51.

Gaffey, S. J., 1984, Spectral Reflectance of Carbonate Minerals and Rocks in the Visible and Near Infrared (0.35 to 2.55 UM) and its Applications in Carbonate Petrology, University of Hawaii, 259 p.

Goetz, A.F.H., G. Vane, J.E. Solomon, B.N. Rock, 1985, Imaging Spectrometry for Earth Remote Sensing: Science, 228, 1147-1153.

Harraden, C.L., B.A. McNulty, M.J. Gregory, J.R. Lang, 2013, Shortwave Infrared Spectral Analysis of Hydrothermal Alteration Associated with the Pebble Porphyry Copper-Gold-Molybdenum Deposit, Iliamna, Alaska: Economic Geology, 108, 483-494.

Kokaly, R.F., R.N. Clark, G.A. Swayze, K.E. Livo, T.M. Hoefen, N.C. Pearson, R.A. Wise, W.M. Benzel, H.A. Lowers, R.L. Driscoll, A.J. Klein, 2017, USGS Spectral Library Version 7: U.S. Geological Survey Data Series 1035, 61p.

Kruse, F.A., 1996, Identification and Mapping of Minerals in Drill Core Using Hyperspectral Image Analysis of Infrared Reflectance Spectra: International Journal of Remote Sensing, 17, 1623-1632.

Lyon, R.J.P., F.R. Honey, 1990, Direct Mineral Identification with Geoscan Mk II Advanced Multispectral Scanner (AMSS) in SPIE Proceedings Imaging Spectroscopy of the Terminal Environment, 1298, 50-61.

Martini, B.A., K. Conroy, R. Carey, 2015, Tracking mica chemistry in copper porphyry using core imaging spectroscopy, in Proceedings of International Applied Geochemistry Symposium, Tucson, AZ, USA, 12p.

Mason, P., J.F. Huntington, 2010, HyLogger 2 components and pre-processing: an overview in Munson T., K. Johnston (Eds.), Technological Note 2010-001, Northern Territory Geological Survey, Darwin, 9.

McLeod, R.L., Gabell, A.R., Green, A.A., Gardavsky, V., 1987. Chlorite infrared spectral data as proximity indicators of volcanogenic massive sulfide mineralisation. In: Proceedings of Pacifc Rim Congress 87, Gold Coast, Australia, 321-324.

Orovan, E.A., 2016, Geology, geochemistry and genesis of the Namosi porphyry Cu-Au deposits, Fiji: PhD Geology, University of Tasmania.

Swayze, G.A., R.N. Clark, A.F.H. Goetz, K.E. Livo, G.N. Breit, F.A. Kruse, S.J. Sutley, L.W. Snee, H.A. Lowers, J.L. Post, R.E. Stoffregen, R.P. Ashley, 2014, Mapping Advanced Argillic Alteration at Cuprite, Nevada Using Imaging Spectroscopy: Economic Geology, 109, 1179-1221.

Roache, T. J., J. L. Walshe, J. F. Huntington, M. A. Quigley, K. Yang, B. W. Bil, K. L. Blake & T. Hyvärinen, 2011, Epidote–clinozoisite as a hyperspectral tool in exploration for Archean gold, Australian Journal of Earth Sciences, 58:7, 813-822.

Scott, K.M. and Yang, K., 1997. Spectral reflectance studies of white micas. (CSIRO/Amira P435) CSIRO Exploration and Mining Report 439R, 35pp.

Tappert, M.C., B. Rivard, R. Tappert, J. Feng, 2013, The mineral chemistry, near-infrared, and mid-infrared reflectance spectroscopy of phengite from the Olympic Dam IOCG deposit, South Australia: Ore Geology Reviews, 53, 26-38.

Vane, G., R.O. Green, T.G. Chrien, H.T. Enmark, E.G. Hansen, W.M. Porter, 1993, The airborne visible/infrared imaging spectrometer (AVIRIS): Remote Sensing of Environment, 44, 127-143.